Electrochemical Doping in Ordered and Disordered Domains of Organic Mixed Ionic-Electronic Conductors

Priscila Cavassin, Isabelle *Holzer, Demetra Tsokkou, Olivier Bardagot, Julien Réhault, Natalie Banerji**

P. Cavassin, I. Holzer, Dr. D. Tsokkou, Dr. O. Bardagot, Dr. J. Réhault, Prof. N. Banerji

Department of Chemistry, Biochemistry and Pharmaceutical Sciences, University of Bern, Freiestrasse 3, 3012 Bern, Switzerland

E-mail: natalie.banerji@unibe.ch

Conjugated polymers are increasingly used as organic mixed ionic-electronic conductors in electrochemical applications for neuromorphic computing, bioelectronics and energy harvesting. The design of efficient electrochemical devices relies on large modulations of the polymer conductivity, fast doping/dedoping kinetics, and high ionic uptake. In this work, structure-property relations are established and control of these parameters by the co-existence of order and disorder in the phase morphology is demonstrated. Using *in-situ* time-resolved spectroelectrochemistry, resonant Raman and terahertz conductivity measurements, the electrochemical doping in the different morphological domains of poly(3-hexylthiophene) is investigated. The main finding is that bipolarons are found preferentially in disordered polymer regions, where they are formed faster and are thermodynamically more favoured. On the other hand, polarons show a preference for ordered

domains, leading to drastically different bipolaron/polaron ratios and doping/dedoping dynamics in the distinct regions. A significant enhancement of the electronic conductivity is evident when bipolarons start forming in the disordered regions, while the presence of bipolarons in the ordered regions is detrimental for transport. This study provides significant advances in the understanding of the impact of morphology on the electrochemical doping of conjugated polymers and the induced increase in conductivity.

1. Introduction

Electrochemical doping is one of the most efficient and controlled ways to tune the conductivity of organic semiconductors by several orders of magnitude.[1] Because this doping process is reversible, it allows precise modulation of the conductivity level, making it an important tool for a wide range of novel applications, such as neuromorphic systems,[2] thermoelectric generators,[3] batteries,[4] and organic electrochemical transistors (OECTs) for biological interfacing.[5] In electrochemical doping, electronic charge carriers are injected into the organic thin film from an electrode, while counterions from an electrolyte infiltrate the film to maintain charge neutrality. The magnitude of the voltage applied between the film and a counter electrode tunes the conductivity by controlling the density of charge carriers in the film.[6] When the film becomes positively charged, this is referred to as p-type doping or alternatively as oxidation with simultaneous compensation by negative ions.

Ideal organic electrochemical devices require fast doping and depoping kinetics (*i.e.,* fast ON/OFF switching) combined with high ionic uptake (*i.e.,* high capacitance), and high conductivity (*i.e.,* high doping levels and high mobility of the electronic carriers). Both the intrinsic material properties and the morphology of the film need to be fine-tuned to simultaneously optimize these parameters. This requires clear structure-property relations that are currently not well understood. Here, we investigate electrochemical doping of the archetypal conjugated polymer poly(3-hexylthiophene) (P3HT) by *in-situ* spectroelectrochemical techniques probed in the visible-near-infrared (Vis/NIR), Raman and THz range. We correlate the generation dynamics of different charged species (polarons,

WILEY-VCH

bipolarons) in distinct morphological domains to the nanoscale conductivity at different doping levels.

Most conjugated polymers are indeed semi-crystalline, with a mixture of ordered and disordered domains in thin films. This heterogeneity impacts the doping process and considerably complicates its characterization, as highlighted for P3HT in recent X-ray diffraction studies.[7] For instance, Guardado *et al*. and Thomas *et al*. have independently demonstrated that at low electrochemical doping levels, ions are preferentially located in the disordered domains of P3HT despite polarons being formed in the more ordered domains. [7f, 8] It is only at high doping levels that ions also penetrate the ordered domains. A drawback of these studies is that X-ray diffraction accesses only the crystalline domains of the film. Alternatively, *in-situ* electrochemical resonant Raman spectroscopy (ERRS) is sensitive to subtle changes in the polymer backbone conformation, so that it can distinguish neutral and charged species in the ordered and disordered regions. Nightingale *et al.* have used this technique to show that the ordered polymer domains undergo more pronounced changes in molecular conformation when they are doped.[7g] However, bipolarons were not considered in this study and are often ignored in electrochemical investigations of P3HT.[7a, 7e, 7f, 8] They are nevertheless present at high doping levels and their Raman signatures were recently discussed by Mansour *et al.* in molecularly doped P3HT.[9] We, as well as Neusser *et al.*, have demonstrated that those bipolarons play an important role in the conductivity of the electrochemically doped polymer.[7d, 10] Now, further understanding on how the presence of polarons and bipolarons in different morphological domains impacts the transport is essential, and therefore it is critical to differentiate between the doping mechanisms that take place in each region of P3HT films.

In this work, we offer novel insights on: i) the generation of polarons and bipolarons in the distinct domains, ii) the doping of the disordered domains, which has been much less explored, iii) the kinetics of the redox reactions involved at various doping and dedoping levels, and iv) the impact of having different carriers in the ordered and disordered regions on the short-range transport

WILEY-VCH

properties. We find that in contrast to polarons, bipolarons are preferentially found within disordered domains, which by themselves have low conductivity. Nevertheless, the high charge density stored as bipolarons in these regions is beneficial to the overall transport up to a critical bipolaron concentration. We demonstrate that all aspects of electrochemical doping in conjugated polymers (ionic and electronic doping level, degree of oxidation, doping and dedoping kinetics, conductivity) differ significantly in the ordered and disordered regions of the film and can be controlled by tuning their co-existence. This provides opportunity for materials design and morphological optimization.

2. Results and discussion

2.1 Evolution of the redox species at different voltages

We first measure the absorbance changes of a P3HT thin film (~ 20 nm dry thickness) immersed in aqueous KPF_6 electrolyte (0.1 mol L^{-1}) at different electrochemical doping potentials. Efficient electrochemical doping of P3HT in this electrolyte has been previously reported.[11] For those spectroelectrochemistry measurements, we use a home-built setup that applies a square voltage pulse and simultaneously measures the current response and the visible to near infrared (Vis/NIR) absorbance of the film (**Figure 1a**). The films are spin-coated on a conductive ITO substrate from chloroform solution, yielding a relatively disordered morphology.[12] The voltage is applied on the Ag/AgCl electrode ranging from +0.2 V to -0.8 V, with steps of 0.1 V. In this article, in view of future applications, all voltages are expressed using the transistor convention where the working ITO/P3HT electrode is grounded and the potentials are applied at the Ag/AgCl quasi-reference (gate) electrode. As a result, the voltage signs are opposed compared to typical electrochemistry convention, i.e. negative voltage induces oxidation (doping) and positive voltage induces reduction (dedoping) of P3HT. Before each measurement, five doping/dedoping cycles are performed to stabilize the response. In Figure 1b, the evolution of the spectra at different voltages is displayed. The corresponding injected charge (determined from chronoamperometry) is depicted in Figure S2. Initially, the absorbance is centered around 500 nm, but as the applied voltage becomes more negative, we observe a decrease of this band concomitant with the rise of a band around 800 nm,

WILEY-VCH

followed by the rise of another band around 1400 nm at the most negative voltages. To deconvolute the overlapping absorbance signatures and their evolution with the applied voltage, we use Multivariate Curve Resolution (MCR) analysis (Figure S1). We find that the absorption spectra can be decomposed into four different spectral signatures (Figure 1c). The data reconstruction from the spectral components (MCR fit) is shown in Figure S1. Their absorbance cross section is estimated by relating the absorbance to the density of injected charge, measured by chronoamperometry on films of different thicknesses (Note S2, Figure S2, Table S1).

The absorption around 500 nm is attributed to P3HT in the neutral state. The MCR analysis decomposes this neutral band into two distinct spectral signatures (Figure 1c): i) The neutral polymer in more disordered regions (amorphous phase), which has a broad Gaussian-like peak centered at 495 nm, and ii) the polymer in more ordered domains of the film (crystalline phase), that exhibits the two characteristic 0-0 and 0-1 vibronic bands centered at 560 nm and 605 nm. Both spectral signatures are similar to the absorption spectra of disordered and ordered P3HT that have been directly measured and reported in the literature.[13] The suppressed 0-0 vibronic band compared to the 0-1 peak in the spectrum of ordered regions points to weak H-like aggregation between the polymer chains. By calculating the A_{0-0}/A_{0-1} peak ratio (= 0.86), the interchain coupling can be estimated to $\approx$ 34 meV,[13c] which is an intermediate value suggesting packing between chains with significant intrachain order.

Also in agreement with previous studies, the spectral components at 800 nm and 1400 nm are assigned to singly and doubly charged species.[7c, 7d] Upon oxidation of P3HT, a single electron is removed from the polymer chain and a localized lattice distortion occurs. Together, they are defined as a positive polaron.[7c, 14] When another electron is removed from the P3HT chain, either a coupled polaron pair forms (triplet multiplicity), or both polarons share the same local lattice distortion resulting in a bipolaron (singlet multiplicity).[14] Theoretical work suggests that mostly bipolarons are found in electrochemically doped P3HT, as the counterions can come close enough together to stabilize both charges.[14b, 15] This is consistent with electron paramagnetic resonance (EPR)

5

WILEY-VCH

measurements, which show a decreasing signal due to unpaired spins at high oxidation potentials.[7c, 7d] Therefore, we assign the doubly charged P3HT segments to bipolarons. Recent electronic structure calculations, using for example density functional theory (DFT), have led to a significantly revised picture of the optical transitions of doped polymers compared to the traditional description, which neglects Coulomb interactions.[14-16] Even within the DFT formalism, discrepancies exist concerning the assignment of the spectroscopic bands at 800 nm and 1400 nm in P3HT. According to Sahalianov et al., both bands contain contributions of polarons and bipolarons, which shift and change intensity according to the oxidation level.[15] On the other hand, Wu at al. attribute the band at 800 nm to polarons and the one at 1400 nm to bipolarons,[14b] similar as in the traditional picture and in agreement with most experimental reports. We adopt the latter assignment, as it is consistent with the distinct evolution of the two bands with voltage (Figure 1) and time (section 2.3), leading to the isosbestic point around 950 nm and allowing deconvolution by MCR. Moreover, the bands correlate to the corresponding Raman bands of polarons and bipolarons (section 2.2).

Figure 1d shows how the density of each redox species (obtained from the MCR concentrations and absorbance coefficients) evolves with applied voltage. We note that this density refers to the dry film volume, but it is known that hydrophobic P3HT undergoes little swelling when immersed in water or electrochemically doped with KPF_6 (only about 1.5%).[11, 17] We distinguish four different doping regimes. Between +0.2 V and 0 V (regime 0), there is no significant change in the spectra, which indicates an oxidation onset at 0 V in aqueous 0.1 mol L^{-1} KPF_6 electrolyte. In regime 0, mainly neutral species are present, whereby our analysis shows that the film is composed of about 57% disordered and 43% ordered sites, in accordance with literature for similar molecular weight and coating conditions.[18] Note that the electrochemical pre-cycling of the film results in a non-zero density of polarons below the oxidation onset, likely because a few ions are trapped inside the film.[19] From 0 V to -0.2 V (regime I), there is a decay of both ordered and disordered neutral species concomitant with the rise of the polaronic population. Between -0.3 V to -0.5 V (regime II), both the populations of polarons and bipolarons are increasing while the neutral signatures further decrease. Finally, for voltages more negative than -0.5 V (regime III), the ordered neutral population is completely depleted, while the disordered neutral population continues to decay. This suggests a

WILEY-VCH

lower oxidation potential for the neutral ordered species (crystalline phase) compared to the amorphous phase, as previously reported.[7f, 8, 20] The fact that the distinct morphological domains dope at different voltages leads to the apparent blue-shift of the absorption band around 500 nm (Figure 1b).[7c, 7f] Moreover, in regime III, the bipolaron density continues to increase, while the polaron density decreases, suggesting that part of the polarons is converted to bipolarons.[7c] At -0.8 V, the film is completely doped and contains predominantly polarons (47%) and bipolarons (53%).

Summing the density of all species shows that the total density increases at the negative doping voltages, in particular when bipolarons are being formed (Figure 1d). The neutral species correspond to chromophoric units (ground state polymer segments responsible for light absorption), while the charged species are structurally modified polymer segments from which one or two electrons have been removed. Based on the reported film density of P3HT,[21] the density of monomers is around 4×10^{21} cm^{-3}. Relating this to the total density of neutral species at +0.2 V (5.3×10^{20} cm^{-3}, Figure 1d), we find that the chromophores extend roughly over 7-8 monomers. Since the total density stays constant when neutral species are converted to polarons (regime I), we conclude that the polarons have a similar spatial extent as the neutral chromophores. However, at -0.8 V about twice the density of bipolarons is formed compared to what is expected from a one-to-one conversion from polarons, implying that bipolarons are more localized and span only 4 monomers.

2.2 Structural backbone changes during electrochemical doping

Although some spectral changes for localized and delocalized charges of doped P3HT in solution have previously been reported,[22] the broadness of the polaron and bipolaron bands in our Vis/NIR spectroelectrochemistry film data does not allow to distinguish whether those species are present in the ordered or disordered domains of P3HT. Therefore, we switch to *in-situ* electrochemical resonant Raman spectroscopy (ERRS), which is more sensitive to the structure and environment of the polymer backbone.[7g] For experimental reasons, the P3HT film (thickness of approximately 40 nm) is now spin-coated on two short-circuited gold electrodes separated by a 2 mm gap ('OECT-like' device), unlike the planar ITO-based sample of the previous section. The device is immersed in the

electrolyte together with the Ag/AgCl electrode and the Raman spectra are acquired after reaching the steady state for voltages ranging from +0.2 V to -0.8 V with steps of 0.1 V. The excitation wavelength used is 633 nm, which is mainly resonant with the ordered neutral absorption band of P3HT. Thus, the Raman intensity strongly decays as ordered P3HT is depleted, so that the spectra are normalized in order to compare the changes upon doping (Figure S3).

The normalized Raman spectra at selected voltages are shown in **Figure 2a**. We assign the observed bands based on previous Raman studies on doped and undoped P3HT.[7g, 9, 23] When the film is undoped (V > 0 V), the Raman spectra show an intense band at 1455 cm^{-1} and a weaker band at 1380 cm^{-1}, attributed to the $C_\alpha - C_\beta$ and to the $C_\beta - C_\beta$ stretching vibrations, respectively (see inset of Figure 2a).[7g, 23] When the film is doped and predominantly polarons are formed (-0.2 V to -0.5 V), the $C_\alpha - C_\beta$ vibrational mode shifts towards smaller wavenumbers to the 1405-1438 cm^{-1} region.[7g, 23] This shift is due to a more planar backbone and more delocalized π-electrons in the polaronic state. Nightingale *et al*. have combined DFT calculations and ERRS to demonstrate that the $C_\alpha - C_\beta$ bands of neutral and polaronic P3HT consist of a convolution of signals from ordered and disordered domains.[7g] For neutral P3HT, disordered chains vibrate at higher frequency than more ordered chains due to a shorter conjugation length. Conversely, polaronic disordered chains vibrate at a lower frequency than ordered ones, since the ordered segments undergo weaker lattice distortions compared to the large conformational changes when polarons form in disordered P3HT.[7g] When we go to even higher doping levels where bipolarons are generated (< -0.5 V), two peaks appear at 1465 and 1493 cm^{-1}. Mansour *et al.* have chemically doped P3HT and observed bipolaronic peaks at similar wavelengths.[9] They have assigned the peak at ~1460 cm^{-1} to the $C_\alpha - C_\beta$ symmetric stretching mode of disordered bipolarons, and the one at ~1500 cm^{-1} to the $C_\alpha - C_\beta$ asymmetric stretching, which appears when high disorder is induced at high chemical doping levels. Unlike for chemical doping, the electrochemical oxidation of P3HT does not necessarily lead to enhanced disorder. Moreover, in our data, we observe that the peak at 1493 cm^{-1} appears only in regime III, when ordered polarons are converted to bipolarons. Therefore, we rather assign this band to the formation of bipolarons in the ordered domains. The blue-shift of both

WILEY-VCH

bipolaron bands has been previously attributed to a shorter conjugation length,[9] in full agreement with our observation that the bipolarons are about twice as spatially localized as the neutral and polaron sites.

Following the procedure of Nightingale *et al.*,[7g] we use Gaussians to deconvolute the signature of the $C_\alpha - C_\beta$ stretching mode into contributions of ordered and disordered species in different redox states (Figure 2a, Figure S4 and Table S2). As seen before with Vis/NIR spectroelectrochemistry, some polarons are already present at 0 V (regime 0) and this effect is slightly enhanced in the OECT-like configuration. The ERRS analysis now allows to assign those trapped polarons to the ordered regions of the film. At -0.5 V (regime II), a strong decrease of both the ordered and disordered neutral signatures, an increase of the polarons in both regions and a rise of the disordered bipolarons are observed. Finally, at -0.8 V (regime III), the signal from polarons in the ordered domains decreases while the ones from the disordered polarons and bipolarons in both domains rise. We note the presence of neutral segments even at the highest doping voltages, in contrast to the data in Figure 1. This could be related to less efficient doping in the OECT-like geometry or to enhancement of the neutral bands due to their resonance at 633 nm.[24]

The area of the deconvoluted peaks give us insights about the evolution of the species upon doping. Figure 2b depicts the relative peak area (normalized by the total peak area summed over all Gaussians) for the different redox species as a function of the applied voltage. The data corroborates that the ordered neutral regions are oxidized at slightly lower potential than the disordered ones. Additionally, ERRS demonstrates that polaron formation in the ordered domains occurs before that in the disordered domains. The opposite trend is seen for the bipolarons, which form in the disordered domains at less negative voltages. Although we did not correct for the oscillator strength of the Raman bands, it is remarkable that their sum reproduces extremely well the evolution of the different neutral and charged species measured by Vis/NIR spectroscopy (measured on the same OECT-like device as the ERRS, Figure 2b and Figure S5). This validates our interpretation for both spectroscopic techniques and confirms the observed trends. An important conclusion from ERRS is

WILEY-VCH

that charge carriers remain in both the ordered and disordered domains once steady-state conditions are reached (in the absence of applied source-drain voltage). We cannot exclude a dynamic equilibrium between the charges in different morphological regions, but the overall charge density of polarons and bipolarons stays in the region where it was initially generated.

2.3 Dynamics of the electrochemical reactions

Time-resolved spectroelectrochemistry in the Vis/NIR range allows to go beyond the steady-state response and to monitor the dynamics of the electrochemical doping. This is key to understand the mechanisms of the redox processes and how they differ for the distinct morphological domains. Using the same experimental setup shown in Figure 1a and the planar ITO-based device, we measure the spectral response to a square voltage pulse with a time resolution of 10 ms, much higher than what can be achieved by state-of-the-art X-Ray scattering techniques.[7b] Each voltage pulse occurs from +0.4 V (dedoping voltage) to a doping voltage that is stepped down from -0.1 V to -0.8 V and back to +0.4 V (Figure S6). Figure S7 shows the dynamics for P3HT films with 4 different thicknesses (5, 20, 55 and 110 nm) for a doping voltage of -0.8 V. The dynamics of the thicker films gradually slow down and become less exponential, with the lifetime (to reach 1/e of the initial signal amplitude) increasing sub-linearly with film thickness (Figure S7). Here, the doping dynamics is likely limited by the time it takes for the electrolyte anions to penetrate throughout the film.[25] However, the dynamics converge to an almost similar time evolution for the thinner films of 20 nm and 5 nm thickness. In this range, the ionic transport likely has a small impact on the dynamics, i.e. ions are present in the film faster than the redox reactions. This is in agreement with recent work showing that the mass transport of ions can be faster than the population kinetics of the electronic charges.[26] We observe therefore the intrinsic oxidation rates that dope P3HT (including hole injection, hole transport across the film and structural rearrangements). This is in the focus of the current work, and therefore a thin film of 20 nm is used in the following analysis (**Figures 3** and **4**).

The temporal evolution of the density of disordered neutral, ordered neutral, polaron and bipolaron species (from MCR decomposition with the components in Figure 1c) is depicted in Figure 3 for

WILEY-VCH

representative doping and dedoping processes in regime I (-0.2 V), regime II (-0.5 V) and regime III (-0.8 V). For a first assessment of the data, we estimate the rate constants of the electrochemical doping and dedoping processes by using a sum of exponentials to fit the dynamics (Note S3 and S4, Figure S8 to S11, Table S3 and S4). Typically, we require two exponentials to describe the conversion between redox species, as well as offsets (equal to the steady-state densities) that represent the equilibria establishing between the species at each voltage. The faster component usually accounts for about 80-90% of the conversion. The biexponential behaviour can be explained by some structural and energetic inhomogeneity of the polythiophene chains in the ordered and disordered regions.[27] Moreover, the doping dynamics at the earliest times cannot always be reproduced with the biexponential function, especially at low doping voltages. We tentatively ascribe this short delay to ions reaching the proximity of the electrochemical reaction site and discard it during the exponential fitting. The effect becomes negligible for the dedoping dynamics.

The kinetic traces in Figure 3 and their exponential analysis reveal clear correlations between the dynamics of the neutral and charged species, allowing to deduce how they interconvert. During doping, the decay of ordered neutral species correlates mainly with the formation of polarons and is slightly faster (at a given voltage) than the decay of disordered neutral species, which is concomitant with the rise of bipolarons below -0.3 V (Table S3). This agrees with the lower oxidation potential of the ordered domains and the preferential formation of bipolarons in amorphous regions.[7f, 7g] The rate of P3HT oxidation (charge transfer with the electrode) accelerates with higher applied voltage. Similar to what was observed in PEDOT:PSS,[28] the increasing overpotential with respect to the oxidation onset increases the driving force of the reaction, by raising the potential of the electrode and stabilizing the oxidation products. For example, the average time constant for the neutral ordered decay evolves from τ = 1.0 s (at -0.3 V) to τ = 0.2 s (at -0.8 V), and the neutral disordered decay accelerates from τ = 2.3 s to τ = 0.9 s within this voltage range. Moreover, the final equilibria shift towards a higher doping level at more negative voltages, with the offsets of the neutral species decreasing and the offsets of the polarons and bipolarons increasing. For the highest doping voltages (-0.6 V to -0.8 V), the polaron population first peaks and then decays with a time constant of $\tau \approx$ 5-6 s

WILEY-VCH

that is correlated with the slower bipolaron rise. We assign this to the conversion of polarons to bipolarons in the ordered regions (see kinetic model below).

For the dedoping, the switch always occurs to a voltage of +0.4 V, so that the final population (dominated by the neutral species) is independent of the initial doping voltage (Figure 3, Table S4). This nevertheless determines the doping level at the start of the process. We find that dedoping is generally faster than doping and occurs by the inverse reactions. Despite starting from varying degrees of oxidation (initial doped state), the rate of the reduction shows only a weak dependence on the voltage jump. This suggests that the dedoping rate is determined by the final equilibrium between polaron and neutral species at constant +0.4 V dedoping voltage. For all regimes, the doping is completely reversible, which indicates that no permanent morphological disruption is induced by the injection of ions in our experimental conditions and after the pre-cycling.[8] When initially present, the bipolarons show a fast decay (τ = 0.1 s from -0.3 V to -0.6 V), which slightly slows down when more bipolarons are present in the ordered domains (τ = 0.2 s from -0.7 V to -0.8 V). At the most negative voltages, a concomitant rise of the polarons is observed. Apart from that, the polarons decay with an average time constant that ranges from 0.4 s to 0.7 s between -0.1 V and -0.8 V, and which correlates to the rise of the disordered neutral species. We note that even the fastest doping and dedoping dynamics measured here for P3HT are at least one order of magnitude slower than the ones we recently reported for the electrochemical reactions of PEDOT:PSS (for a step from +0.1 V to -0.6 V and back).[28] Further experiments to elucidate the slow redox reactions in P3HT are ongoing.

2.4 Kinetic modelling of the reaction mechanisms

Based on these observations, we build a kinetic model to describe the doping and dedoping mechanisms that occur in the different regions of P3HT (Notes S5 and S6, respectively). Such a model confirms the reaction sequence and additionally disentangles the dynamics of the charges in the ordered and disordered regions. The model is implemented using the symfit Python package.[29]

To simplify, we discard the initial non-exponential delay in the doping dynamics at low voltages, and we account only for the predominant fast component of the conversion between the redox species (ignoring the ~10-20% slower component due to inhomogeneity). As closure is required for kinetic modelling, we divide the bipolaron population by 1.37 during the fitting to keep the total species density constant. We know from the Raman data that distinct polarons and bipolarons in the ordered and disordered regions are formed, so that their population is subdivided into ordered and disordered species in the model. The sum is fit to the experimental dynamics. No exchange between the species in the two domains is necessary to obtain a good fit, so we assume that charges stay in the region where they are generated. Finally, to account for the equilibria between redox species at each doping voltage, we introduce back-transfer rates for all processes. The fits to the kinetic model are shown in Figure 3 and Figure S12 to S17. The fit parameters are summarized in **Table 1 and 2** for the doping and dedoping, respectively, and are depicted as a function of the applied voltage in Figure 4.

Regime I (-0.1 V to -0.2 V). Here, neutral species in both ordered and disordered domains are converted to polarons, resulting in equilibria ($N_{dis} \rightleftharpoons P_{dis}$ and $N_{ord} \rightleftharpoons P_{ord}$) between the redox states. At increasing doping voltages, the rate of polaron generation increases and the equilibria shift towards their formation. It has previously been reported using X-ray diffraction, that at such low doping voltages, the electrolyte anions mainly enter the amorphous regions of P3HT, but most of the polarons are formed in the more ordered polymer regions (at the interface to disordered domains, see schematics in Figure 3a).[7f, 8] Unlike for chemical doping, the charge transfer in electrochemical doping takes place with the electrode and not with the counterion, so that they do not necessarily have to come to a reacting distance. It is therefore reasonable that the electric field generated by anions in the disordered regions extends sufficiently far (by several nanometres) to stabilize polarons in nearby ordered regions. Our analysis allows to quantitatively determine that 66% of all polarons are formed within the ordered regions at -0.2 V. The higher equilibrium constant of polaron formation further confirms a spontaneous, thermodynamically favoured (more exergonic) oxidation of the ordered domains. We speculate that this stabilization arises from a combination of i) the lower oxidation potential of the ordered polymer chains, ii) a lower degree of lattice

reorganization upon polaron formation, iii) higher charge delocalization, and iv) favoured charge hopping from the ITO electrode to the doping site due to higher hole mobility. Additionally, we find that the conversion to polarons is about three times faster in the ordered regions. When switching back to +0.4 V from either -0.1 V or -0.2 V, the reduction to the neutral state is 1-2 orders of magnitude faster than the initial oxidation, occurs on a similar time scale in the ordered and disordered regions and shows a weaker dependence on the voltage jump. The conversion to neutral species ($P_{dis} \rightleftharpoons N_{dis}$ and $P_{ord} \rightleftharpoons N_{ord}$) is almost complete, except for a small concentration of polarons remaining in the ordered regions, likely due to trapped ions and lattice changes during the initial pre-cycling.

Regime II (-0.3 V to -0.5 V). The trends from the previous regime continue, with the conversion to polarons becoming faster and more favourable with increasing doping voltage in both morphological regions, and the doping being generally faster in the ordered domains. The total charge density now reaches 4×10^{20} cm^{-3}, which has been reported as the threshold for ion penetration into the ordered regions of P3HT, leading to important crystalline changes and enhanced mobility.[7f, 8] At -0.5 V, about 66% of polarons are formed within the ordered regions and 94% of the ordered neutral density decays according to $N_{ord} \rightleftharpoons P_{ord}$ (Figure 3b). In contrast, only 66% of the neutral disordered segments are converted to charges. Additionally, there is conversion of polarons to bipolarons (increasingly enhanced at more negative voltages), but this occurs only in the disordered domains ($N_{dis} \rightleftharpoons P_{dis} \rightleftharpoons B_{dis}$). The rate of this process is comparable (slightly slower) to the preceding conversion of disordered neutral segments to polarons, so that the disordered neutral decay appears to correlate to the bipolarons rise in the experimental data. In agreement with preferential bipolaron formation in the disordered regions, Nightingale *et al*. suggest that the oxidation peak of the amorphous phase coincides with bipolaron formation.[7g] This is promoted by the higher reorganization energy and charge localization found in disordered P3HT domains.[7g] Moreover, the bipolarons are stabilized by the ions present predominantly in these regions, with the disordered structure possibly favouring two closeby counterions.[14b] Switching back to a dedoping voltage of +0.4 V in regime II leads to very fast and complete back-conversion in the disordered regions

according to $B_{dis} \rightarrow P_{dis} \rightleftharpoons N_{dis}$. In the ordered domains, the reduction of polarons ($P_{ord} \rightleftharpoons N_{ord}$) is slightly slower and slows down with increasing voltage jump.

Regime III (-0.6 V to -0.8 V). At the highest doping voltages, all the oxidation processes in the ordered and disordered regions become even faster and more favourable. The conversion of neutral species to charges is over 97% complete at -0.8 V, even in the disordered domains, where similar densities of polarons and bipolarons are formed according to $N_{dis} \rightleftharpoons P_{dis} \rightleftharpoons B_{dis}$. About 20% of all bipolarons are now also generated in the ordered regions ($N_{ord} \rightarrow P_{ord} \rightleftharpoons B_{ord}$), but at a much slower rate, leading to a relatively low equilibrium concentration. It is noteworthy that this conversion in the ordered domains only starts after all neutral species have been depleted by at least 97%, resulting in a peak of the polaron population before they slowly decay to bipolarons. We have recently reported a similar behaviour in PEDOT:PSS.[28] The penetration of ions into the ordered domains in regime III might be required for bipolarons formation. Upon dedoping (to + 0.4 V), the ordered bipolarons decay about four times faster than the disordered bipolarons, while the conversion of polarons to neutral species is faster in the disordered domains.

The overall evolution of the rate and equilibrium constants with the doping and dedoping voltages is summarized in Figure 4. The faster conversion of neutral species to polarons in the ordered regions, as opposed to the much faster conversion of polarons to bipolarons in the disordered regions, is clearly seen during doping (Figure 4a). For dedoping, the rates follow the opposite trend and are highest for the bipolaron to polaron conversion in the ordered regions, while the subsequent formation of ordered neutral species is slowest. The doping rates (shown on a log scale) show an increase and gradual saturation as the oxidation voltage becomes higher, whereas the dedoping rates slightly decrease when the initial voltage is more negative (except for the ordered polaron to neutral conversion, which first increases and then decreases). We tentatively ascribe this behaviour to the impact of driving force, with a more detailed analysis planned in subsequent work. Finally, $\ln(K)$ for all doping processes increases linearly with voltage (Figure 4b), as expected according to Nernst equation. The equilibrium constants clearly highlight that polarons are thermodynamically

WILEY-VCH

more favoured in the ordered regions, while bipolarons prefer the disordered ones. A quantitative analysis is however not possible, as the electrode potentials were not rigorously controlled in the absence of a third reference electrode.

2.5 Impact of film morphology on the redox processes

To verify the impact of the ordered and disordered domains on the electrochemical doping of P3HT, two additional samples with slightly higher order (regioregular P3HT spin fast from o-dichlorobenzene solution) and with much lower order (regiorandom RRa-P3HT cast from chloroform) are investigated. The absorption spectra of the dry films in Figure S18 show that the 0-0 vibronic shoulder is enhanced and the spectrum red-shifted in the regioregular film cast from o-dichlorobenzene compared to the one cast from chloroform. We expect this morphology to be essentially maintained in the KPF_6 electrolyte, since there is relatively little swelling of P3HT in water and the PF_6^- anions can intercalate into free volumes of the film in both the disordered and ordered regions.[7f, 8, 11] On the other hand, the RRa-P3HT film is essentially amorphous, as confirmed by the absence of any vibrational structure. Moreover, the absorbance band of RRa-P3HT is notably blue-shifted, which is attributed to a shorter conjugation length, higher disorder and reduced intermolecular interactions.[30]

The steady-state spectroelectrochemical data obtained in the Vis/NIR range for the regioregular P3HT films cast from o-dichlorobenzene and chloroform is compared in **Figure 5a** and Figure S19 (measured in OECT-like configuration on 35 nm thick films in 0.1 M aqueous KPF_6 electrolyte). The same MCR components as before are used for the analysis. The overall evolution of the redox species with voltage is comparable in the two samples, but some clear differences are seen. First, there are more ordered compared to disordered neutral chromophores initially present in the film cast from o-dichlorobenzene, as expected for more crystalline P3HT. Moreover, more polarons and less bipolarons and are formed upon doping this film, with a bipolaron/polaron ratio of 0.70 at -0.8 V compared to 0.97 for the more disordered film cast from chloroform. This confirms preferential bipolaron formation in disordered regions of P3HT and shows that the bipolaron/polaron ratio in the doped state can be controlled by tuning the morphology. Finally, we notice a high initial polaron

WILEY-VCH

concentration at positive voltages, which is related to the experimental conditions (OECT-like device, shorter dwell time). The effect is more pronounced in the chloroform sample, possibly because trapping of ions is enhanced in the more amorphous film.

The absorbance at different voltages for the RRa-P3HT sample (Figure 5b) is recoded on a 125 nm thick film spin-coated on an ITO substrate and doped with 0.1 M KPF$_6$ in acetonitrile electrolyte. Unlike regioregular P3HT, RRa-P3HT cannot be doped using aqueous KPF$_6$. Because of the electrolyte change, the electrochemical window is shifted to a doping threshold at -0.7 V *vs* Ag/AgCl and a maximum doping level at -1.4 V. Within the investigated window, we never reach a regime where all neutral species are oxidized and there is no significant drop in polaron population, which reaches a constant value while the bipolarons still keep rising (Figure S20). Significantly different MCR signatures are found for RRa-P3HT (Figure 5c). Only disordered and no ordered neutral species are present, with a very blue-shifted band at 400 nm. The polaron and bipolaron spectra are also blue-shifted due to the enhanced disorder, so that two polaronic transitions can now be seen within the spectral window. The blue shift might also indicate that the PF$_6^-$ anions are located closer to the polymer backbones in amorphous P3HT.[31] The time-resolved optical response shown in Figure 5d is measured while applying a voltage of -1.2 V to the RRa-P3HT film. The neutral state decays with a concomitant rise of the polarons and a slower rise of the bipolarons (Note S6, Figure S21, Table S5). The conversions can be kinetically modelled using $N_{dis} \rightleftarrows P_{dis} \rightleftarrows B_{dis}$ (Figure S22, Table S6). Although the film is thicker, we do not expect ionic transport to become a limiting factor, since this is very efficient in amorphous P3HT. The rate and equilibrium constants are $k_{N,dis \to P,dis} = 1.94\ s^{-1}$ (with $K_{N,dis \rightleftarrows P,dis} = 1.1$) and $k_{P,dis \to B,dis} = 0.36\ s^{-1}$ (with $K_{P,dis \rightleftarrows B,dis} = 0.3$). The dynamics is similar to the disordered regions of regioregular P3HT for a similar overpotential (- 0.6 V), also depicted in Figure 5d. This shows that we reach here the intrinsic electrochemical kinetics of amorphous P3HT.

2.6 Short-range conductivity of electrochemically doped P3HT

WILEY-VCH

We have previously shown using terahertz (THz) spectroscopy that the coexistence of polarons and bipolarons is essential to maximize the short-range conductivity of electrochemically doped P3HT.[32] The conductivity was found to first increase with bipolaron concentration and then to plateau or to decrease. Similar findings for the macroscopic conductivity were reported by Neusser *et al.* for the same system.[7d, 32] The behavior was attributed to mixed valence conduction where transport occurs by hole hopping between polaronic and bipolaronic sites.[33] In addition, we can now evaluate the effect of having bipolarons in the ordered and disordered regions. The impact of charges in different morphological domains on the conductivity of electrochemically doped P3HT has not been previously addressed.

We revisit here data that we have initially presented as part of a THz study on P3HT.[32, 34] To obtain a measurable conductivity during electrochemical oxidation, without obstruction of the THz beam by the electrodes, a thicker polymer film (270 nm cast from 1,2-dichlorobenzene) and an OECT-like sample configuration with a 4 mm gap between the gold electrodes is used. THz and Vis/NIR data recorded in 0.1 M $TBAPF_6$/acetonitrile electrolyte is presented, where a higher doping level can be reached than in aqueous KPF_6 (**Figure 6**). We have presented the THz results in water in our previous study, and they do not significantly differ from acetonitrile, except that the high doping levels of interest here cannot be reached in the experimental conditions.[32, 34] The evolution of the Vis/NIR bands is similar in the two electrolytes (Figure S23), but the onset of bipolaron formation shifts to about -0.8 V in acetonitrile (instead of -0.2 V in water). The MCR analysis is carried out with the components and absorption cross sections used throughout this manuscript, showing that the same polaron and bipolaron species are formed in acetonitrile. Apart from the shift of onset potential, a similar evolution of the redox species with voltage is obtained as in Figure 1d, allowing to assign the different doping regimes in the THz sample (Figure 6a). The short-range conductivity at 1 THz starts to be detectable in regime II, when bipolarons are being formed in the disordered regions, and continues to rise into regime III, where the bipolaron concentration increases in both the disordered and ordered domains. However, at -1.4 V, the conductivity saturates and then drops.

WILEY-VCH

The conductivity depends on the effective THz mobility and the conductive charge density, which are disentangled using the Drude-Smith model as previously described (Figure 6a).[32] The mobility shows a weak initial rise, but then stays constant and does not correlate with the evolution of the conductivity. On the other hand, the conductive charge density follows a similar trend as the conductivity and drops at the highest oxidation voltages. The linear correlation of the conductivity to the density of conductive charge confirms the predominant role of charges contributing to transport (Figure 6b). The conductivity decreases at high doping levels although more charges keep being injected, because the fraction of conductive charge with respect to injected charge drops from 42% to 27%. In the investigated voltage range, charge injection leads predominantly to bipolaron formation. The fraction of charges in bipolarons (= 2B/(2B+P), considering two charges per bipolaron) rises linearly with the injected charge density to 71% (Figure 6c). Relating the fraction of conductive charge to the fraction of bipolaronic charge identifies two trends (Figure 6d). First, a linear rise with a slope above 1, showing that every injected charge (converting a polaron to a bipolaron) adds about one conductive charge to the transport. Second, when the bipolaronic fraction reaches 45%, the trend reverses. Adding more bipolarons now linearly decreases the fraction of conductive charge with a slope of -0.8.

In regime II and early regime III, we observe an increase in short-range THz conductivity upon electrochemical doping of regioregular P3HT. In these regimes, we know from the present study that bipolarons are preferentially formed in the disordered regions. Nonetheless, when probing the THz conductivity of RRa-P3HT, no observable THz conductivity is detected, despite the formation of a high density of bipolarons. We can thus assume that the short-range THz conductivity observed in regioregular P3HT is dominated by polaronic charge transport in the ordered regions. Still, we find that the conductivity in the ordered regions is impacted by bipolaron formation in the disordered domains. At the nanoscale, this is likely an interfacial effect, whereby the transport between the ordered and disordered regions is facilitated by holes hopping from disordered bipolarons to ordered polarons, allowing more charges to participate in the short-range transport. The bipolarons might then dissociate to polarons in the ordered regions where they are less stabilized, explaining why we do not observe net bipolaron migration between the domains. These results are in

WILEY-VCH

accordance with reported macroscopic conductivities being at least one order of magnitude higher for regioregular P3HT compared to RRa-P3HT.[7d, 35] Indeed, at the macroscopic scale, the better transport across the ordered/disordered interface is extended along the tie chains that connect the ordered domains.[18, 36] Having a high density (due to their localized nature) and being doubly charged, the bipolarons in the disordered regions represent an important reservoir of charge that favors transport along doped tie chains.

In regime III, the conductivity decreases above a certain bipolaron threshold, which we relate to two effects. First, the concentration of bipolarons in the disordered regions starts to exceed the one of polarons at high oxidation voltages (Figure S13 to S14), which is unfavorable for mixed valence conduction and causes hole-hole repulsions.[37] Second, bipolarons are being formed in the ordered domains, which strongly localizes the charges to a given site. They are stabilized by ions entering the ordered regions, which can cause morphological disruption. The rise of ordered bipolarons at the highest doping levels can therefore also decrease the conductivity.

3. Conclusion

We have applied a variety of *in-situ* spectroscopic techniques to functioning electrochemical devices based on the prototypical P3HT polymer, including time-resolved spectroelectrochemistry, resonant Raman experiments and terahertz conductivity measurements. Our main finding is that the electrochemical doping process differs significantly in the ordered and disordered regions of the film. Thus, bipolarons are found preferentially in disordered polymer regions, where they are formed faster and are thermodynamically more favoured. We relate this to their better stabilization at high ionic content in amorphous P3HT domains, and to higher energetic gain when forming a bipolaron on an initially disordered and localized polymer segment. We provide the following experimental evidence for the effect: i) The polaron-to-bipolaron oxidation onset occurs at lower doping voltage in the disordered compared to the ordered regions (by ~0.2 V). ii) The steady-state bipolaron/polaron equilibrium is more shifted towards bipolarons in disordered domains. iii) The rate of disordered bipolaron formation during doping is about two orders of magnitude higher than for ordered

WILEY-VCH

bipolarons, while the rate of their depletion during dedoping is three times slower. In contrast to bipolarons, polarons show a (less pronounced) preference for the ordered domains, where the neutral-to-polaron oxidation onset is lower, both polaron/neutral and bipolaron/polaron equilibria are shifted more towards polarons, and the polaron formation is faster. Given the opposite preference of polarons and bipolarons for ordered and disordered regions, respectively, we demonstrate that the bipolaron/polaron ratio can be tuned via the morphology in films with different degrees of order.

Amorphous polymer domains are known to favour ionic uptake. Additionally, we show here that they promote the formation of bipolarons, which constitute an important reservoir of electronic charge in the disordered regions. Those bipolarons have a significant impact on transport. An important enhancement of the electronic conductivity occurs when bipolarons start being formed in the disordered regions, caused by an increase of the conductive charge fraction. Since the disordered regions are by themselves not very conductive, we stipulate that the high charge density in the disordered domains helps interfacial transport across ordered/disordered boundaries and along tie chains that connect the ordered domains. At high doping levels, the trend reverses and the conductivity decreases once the density of bipolarons exceeds the one of polarons in the disordered regions (unfavourable for mixed valence conduction), and once bipolarons and ions are present in the ordered regions.

In general, conjugated polymer films are semicrystalline or amorphous, with varying degrees of ordered and disordered regions. We show that all aspects of electrochemical doping (ionic and electronic doping level, degree of oxidation, doping and dedoping kinetics, conductivity) differ significantly in the ordered and disordered domains of the film. The use of organic mixed ionic-electronic conductors in applications such as neuromorphic computing, bioelectronics or energy harvesting depends critically on the control of the electrochemical reactions. The structure-property relations that we have established here illustrate that this control can be achieved by tuning the co-existence of ordered and disordered domains and by exploiting their distinct roles. Thus, the ordered

21

WILEY-VCH

regions afford conductive pathways and fast doping kinetics, while the disordered regions allow to store higher density of charges through the formation of bipolarons and important ionic uptake. Both regions are necessary for high conductivity. We suggest that future materials design aims at controlled two-phase morphologies, for example by the development of dedicated block copolymers containing disordered segments with hydrophilic sidechains as well has segments that form small, interconnected crystallites. Another very promising approach are blends of two materials with complementary properties for optimized electrochemical applications.[38]

4. Materials and methods

Materials: Regioregular P3HT (M1011, Mw = 60,150 g mol^{-1}, 97.6% RR) and glass substrates coated with indium tin oxide (ITO) were purchased from Ossila. Regiorandom RRa-P3HT, chloroform, 1,2-dichlorobenzene (anhydrous) and potassium hexafluorophosphate (KPF$_6$, 99.5%) were purchased from Sigma-Aldrich. An Ag/AgCl pellet electrode (Harvard Apparatus, 1mm diameter) was purchased from Warner Instruments.

Sample preparation: Substrates were cleaned in subsequent ultrasonic baths of Hellmanex (1% vol), bi-distilled water, acetone and isopropyl alcohol, followed by an UV-O$_3$ treatment (20 minutes at room temperature). The P3HT solutions in chloroform were prepared at concentrations of 5, 10, 20 and 40 mg ml^{-1} and stirred at room temperature overnight. The RRa-P3HT solution was also prepared with 10 mg ml^{-1} in chloroform and stirred at room temperature overnight. P3HT solutions in 1,2-dichlorobenzene were prepared with 10 mg ml^{-1} and 40 mg ml^{-1} and stirred at 80°C overnight. All solutions were spin-coated at room temperature on clean substrates (1000 rpm/60 s, THz samples 700 rpm/60s), on glass coated with ITO for the Vis/NIR spectroelectrochemistry and on quartz for the Raman and THz measurements. Beforehand, gold electrodes were evaporated on the Raman and THz substrates (first layer chromium: 10 nm, second layer gold: 60 nm). Precision tip cotton swabs were used to partially remove the film in order to define an area of 12 mm^2 on ITO or to define the channel on the gold patterned substrates. Each sample was then placed in a home-built spectroelectrochemical cell containing both the Ag/AgCl electrode and the electrolyte solution. The spectroelectrochemical results shown in Figure 1 and 3 were performed on a thin P3HT film with

22

WILEY-VCH

about 20 nm thickness and the electrolyte used was 0.1 mol L^{-1} KPF_6 in bi-distilled water. The measurements on RRa-P3HT (~ 120 nm thickness) shown in Figure 5 were performed using 0.1 mol L^{-1} KPF_6 in acetonitrile electrolyte. For the THz measurements in Figure 6 (~ 270 nm film thickness), 0.1 mol L^{-1} $TBAPF_6$ electrolyte in acetonitrile was used.

Vis/NIR spectroelectrochemistry: The spectroelectrochemical measurements were performed using a home-built setup that acquires spectra with a time-resolution of 10 ms.[28] The setup comprises a halogen light source (HL-2000, Ocean Insight), a Flame UV-Vis and a Flame NIR spectrometer (Ocean Insight) triggered by a digital delay/pulse generator (DG535, Stanford Research Systems), and customized Labview code. The voltage between the Ag/AgCl electrode and the film was applied and measured with a data acquisition card (USB-6008, National Instruments, time resolution of 10 ms). The voltages were applied to the Ag/AgCl quasi-reference, and either the P3HT-coated ITO substrate or the gold electrodes on the OECT-like samples were grounded. The transient response current was converted to voltage using a low noise current preamplifier (SR570, Stanford Research Systems) and measured with the same data acquisition card (USB 6008). To increase reproducibility, the P3HT films were cycled four times before the experiments. Each pre-cycle consisted of the application of a -0.8 V pulse for 100 s to dope the polymer followed by the application of a +0.4 V pulse for 100 s to dedope the film. Time-resolved measurements of the transient response of the P3HT films were recorded while applying 100 s square pulses of voltage to subsequently dope and dedope the polymer. The applied voltage for doping ranged between -0.1 V to -0.8 V, with steps of -0.1 V. The dedoping bias was always +0.4 V. For each step of voltage, two square pulses were applied to confirm stability (Figure S6). The time-resolved measurements of the transient response of the RRa-P3HT film were recorded while applying 20 s square pulses of voltage to subsequently dope and dedope the polymer. The dedoping bias was always 0 V. The applied voltage for doping ranged between -0.7 V to -1.4 V, with steps of -0.1 V.

In-situ electrochemical resonant Raman spectroscopy: The ERRS measurements were conducted using a LabRAM HR800 confocal Raman microscope. The samples were irradiated at 633 nm and an excitation power of 9 mW was employed to avoid sample degradation. The accumulation time was of 8 s for each spectrum. First, the frequency of the lines was calibrated using a silicon reference. Then, the excitation light was focused perpendicular on the used cell to allow precise focusing of the

WILEY-VCH

laser on the polymeric film. The samples were prepared as described in the sample preparation, resulting in films with 49 nm thickness and an area of 15 mm^2, whereby 1 mm overlap on each electrode was kept. To increase the reproducibility, the films were cycled four times prior to the experiments. Each pre-cycle consisted in the application of a -0.8 V pulse for 60 s to dope the polymer followed by the application of a +0.4 V pulse for 60 s to dedope the film. The steady-state Raman spectra were measured after applying subsequent -0.1 V voltage steps from +0.2 V to -0.8 V with a dwell time of 100 s. Background emissions were subtracted.

Electrochemical terahertz spectroscopy: For the THz data, the steady-state response was collected after applying subsequent -0.1 V steps for 120 s, from -0.5 V to -1.8 V. We extracted the short-range THz conductivity of electrochemically doped P3HT via time-domain THz transmission spectroscopy. Femtosecond light pulses from a Ti-Sapphire amplifier system (Astrella, Coherent) with a time duration of ~35 fs, 800 nm center wavelength and repetition rate of 1 kHz were used. Part of this near-infrared light beam was focused on a non-centrosymmetric (110) ZnTe crystal to generate the THz pulses via second order non-linear optical rectification. First, the THz beam was focused on the sample position by off-axis parabolic mirrors and then refocused on a second ZnTe crystal, which was used for detection, via free space electro-optic sampling. In the detection crystal, the THz beam spatially and temporary overlapped with a weak part of the fundamental, the gate beam. For this technique, a quarter wave plate, a Wollaston prism and a balanced photodiode were used. The THz propagation through the detection crystal induced a change in the crystal refractive index and the material became birefringent (Pockel effect). This rotated the polarization of the gate beam as it co-propagated with the THz beam through the crystal. The induced ellipticity in the optical pulses was probed by separating the two vertical polarization components with the quarter waveplate and the Wollaston prism, and their difference was measured in the balanced photodetector. The change in gate beam polarization was linearly proportional to the amplitude of the THz electric field. To measure the THz electric field as a function of time, we changed the time delay between gate and THz pulses via a motorized micrometer translation stage. To increase our set-up sensitivity, we used a recent development of the detection scheme, where the polarization of the gate field was biased, allowing more than one order of magnitude increased sensitivity compared with the conventional electro-optic sampling detection scheme.[39] The THz pulses had a duration of about 1 ps and bandwidth between 0.1 and 2.4 THz, where the latter was limited by the phase mismatch in the non-

WILEY-VCH

linear crystals. The THz path was continuously purged with dry nitrogen to eliminate moisture that is strongly absorbed by the THz beam. We were able to extract of the complex optical properties in the ground state. Details about the analysis are described in our previous study.[32]

MCR data analysis: Multivariate Curve Resolution (MCR) analysis was performed on the unprocessed data using *pyMCR*, an open-source software library written in Python.[40] The details of the method are described elsewhere.[40] Briefly, the series of measurements is included in a matrix D, and the goal of the MCR is to solve:

$$D = CS^T + \varepsilon \#(1)$$

where C is the matrix of the species concentrations, S contains their spectral signatures and ε expresses the error, noise or other features of the measurement series that are not taken into account by the fit. The algorithm uses an iterative alternating regression to minimize ε, and to find the best solution for Equation 1. We first used MCR to find the spectral signatures of each species using the data in Figure 1 from the steady-state Vis/NIR spectroelectrochemical measurements and scaled them according to the absorbance cross sections. The same species were then fixed and used throughout the manuscript to determine the concentrations, including for the time-resolved measurements. Subsequently, the dynamics of the species concentrations were fit by a system of ordinary differential equations using the open-source library *symfit*, written in Python (kinetic modelling).[29] The initial guesses for the rate constant were always random values.

Statistical Analysis: To obtain the absorbance cross sections, we compare the absorbance of each species versus injected carrier density for 7 different P3HT films. We observed that the thinner samples (less than 100 nm) do not show consistent values of injected carrier densities. The current we measure is a sum of capacitive, faradaic and leakage contributions. Because the thinner films have less absolute charge participating in the charge transfer process, they are more sensitive to error, and we are likely overestimating the charge density in these films. For this reason, we choose to obtain the absorbance cross section by doing a global fit using the data obtained for only three distinct films, with thicknesses of 110 nm, 130 nm, and 270 nm.

Supporting Information

Supporting Information is available from the Wiley Online Library or from the author.

Conflict of Interest

The authors declare no conflict of interest.

Data Availability Statement

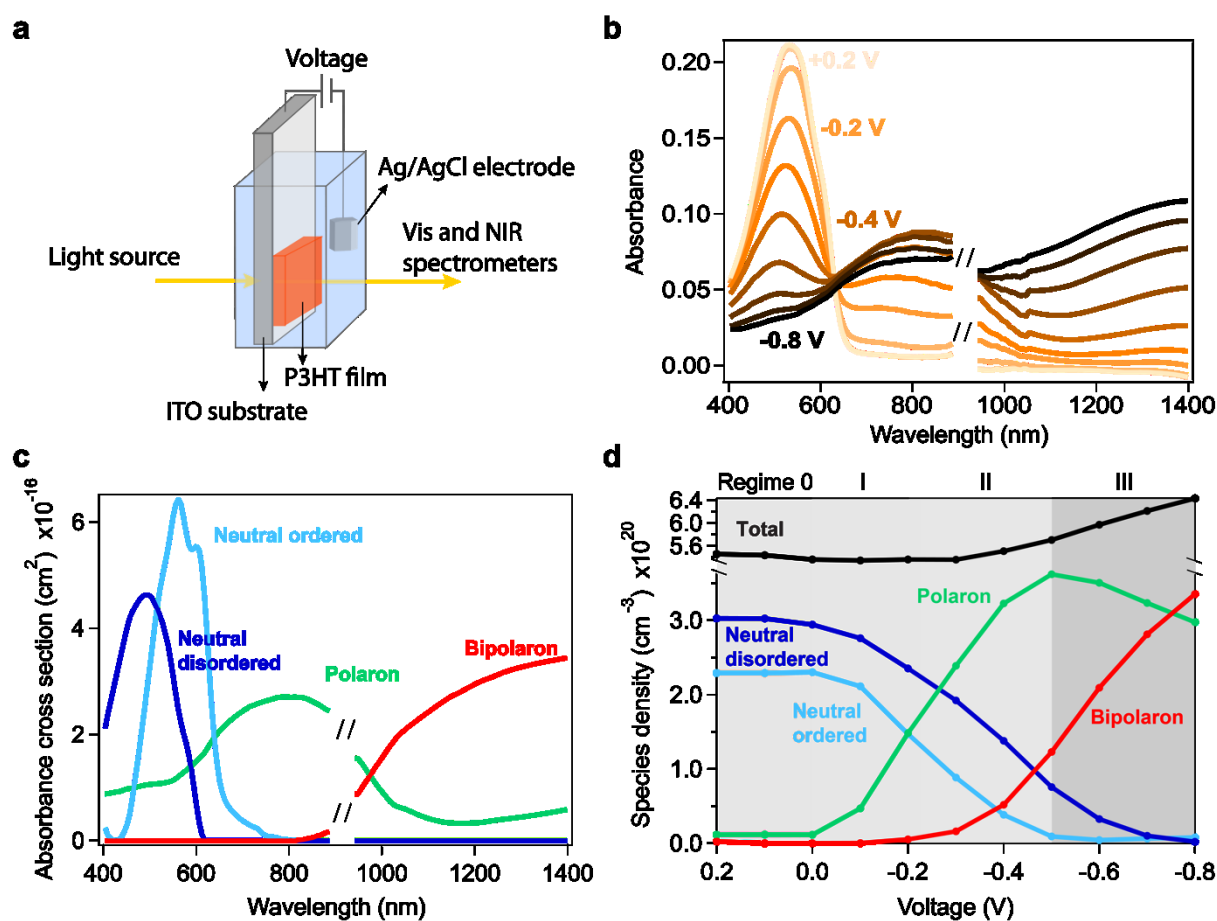The data that support the findings of this study are openly available in the Boris repository of the University of Bern (https://boris.unibe.ch).

Figure 1: a) Experimental setup for the *in-situ* Vis/NIR spectroelectrochemical measurements. b) Steady-state absorbance spectra of P3HT film (cast from chloroform) in aqueous KPF_6 electrolyte (0.1 mol L^{-1}) upon application of doping voltages ranging from +0.2 V to -0.8 V (ΔV = -0.1 V). The region around 900 nm could not be measured (change between Vis and NIR detector). c) Spectral signature and absorbance cross section of each species obtained from the MCR analysis and d) their corresponding densities as a function of the doping voltage.
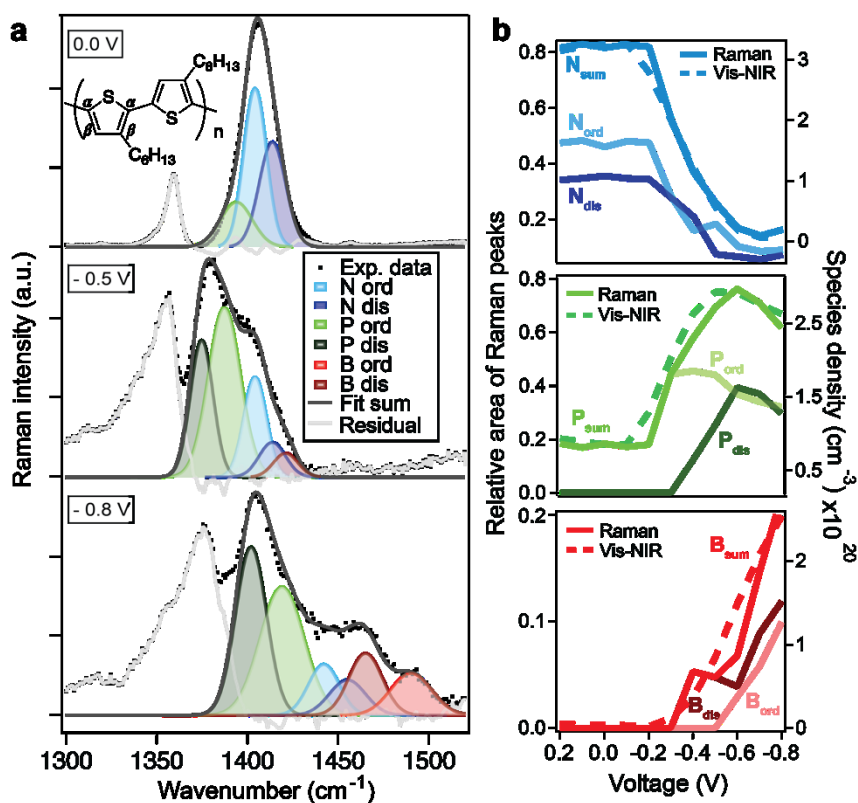
Figure 2: a) *In-situ* electrochemical Raman spectra of P3HT film (cast from chloroform) in aqueous KPF$_6$ electrolyte (0.1 mol L^{-1}) measured in an 'OECT-like' device with excitation at 633 nm. Experimental spectra (dotted lines) and Gaussian deconvolutions (colored curves) are depicted for voltages applied within regime I (0 V), regime II (-0.5 V) and regime III (-0.8 V). b) Evolution of the relative peak areas of the Raman bands of the different redox species in ordered and disordered domains upon doping from +0.2 V to -0.8 V (ΔV = -0.1 V). The evolution of the total neutral, polaron and bipolaron population from Vis/NIR spectroelectrochemistry on the same device is shown for comparison.
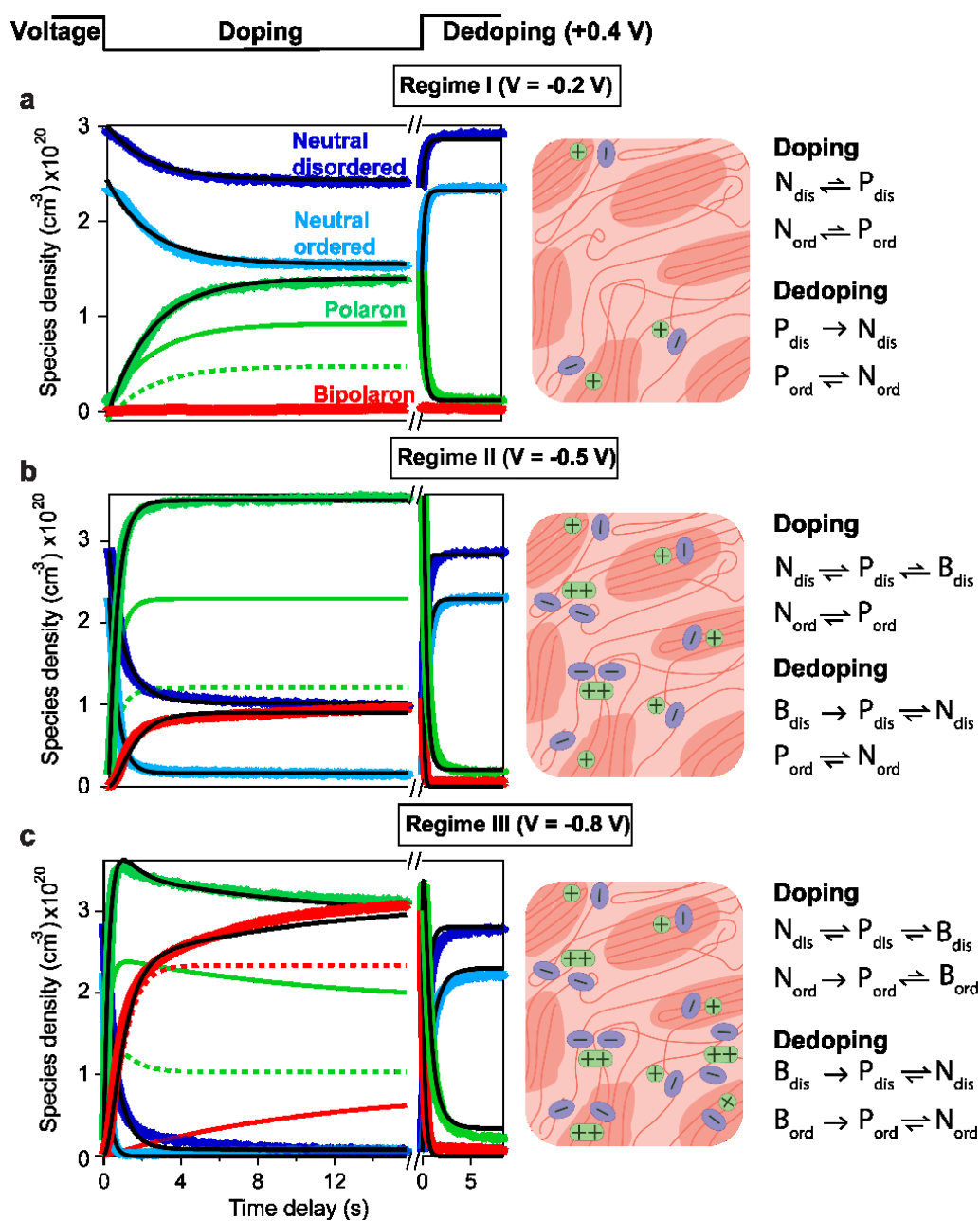
Figure 3: Time-resolved species concentrations obtained from VIS/NIR spectroelectrochemistry of a 20 nm P3HT film (cast from chloroform) in aqueous KPF_6 electrolyte (0.1 mol L^{-1}) upon application of a doping voltage step from +0.4 V to a) -0.2 V, b) -0.5 V and c) -0.8 V (left) and a subsequent dedoping voltage step back to +0.4 V (right). The dynamics are analysed by kinetic modelling

according to the indicated reaction steps (fits shown in black). The simulated ordered (solid line) and disordered (dashed line) subpopulations of polarons (green) and bipolarons (red) are included. For each voltage, a schematic representing the doping in the different morphological domains is depicted (anions in purple and polarons (+) and bipolarons (++) in green).
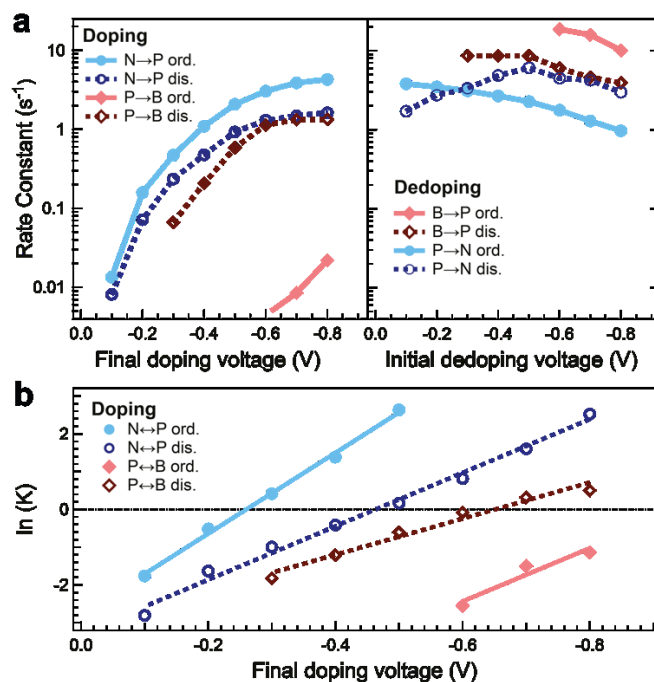

Figure 4: a) Evolution of the rate constants obtained by kinetic modelling of the species dynamics from the VIS/NIR spectroelectrochemistry data of a 20 nm P3HT film (cast from chloroform) in aqueous KPF_6 electrolyte (0.1 mol L^{-1}). The left side shows the doping processes in the ordered and disordered regions of P3HT as a function of oxidation voltage, while the right side shows the corresponding dedoping processes as a function of the initial oxidation voltage (before dedoping to +0.4 V). b) Dependence of the doping equilibrium constants (from the kinetic modelling) on the applied oxidation voltage.
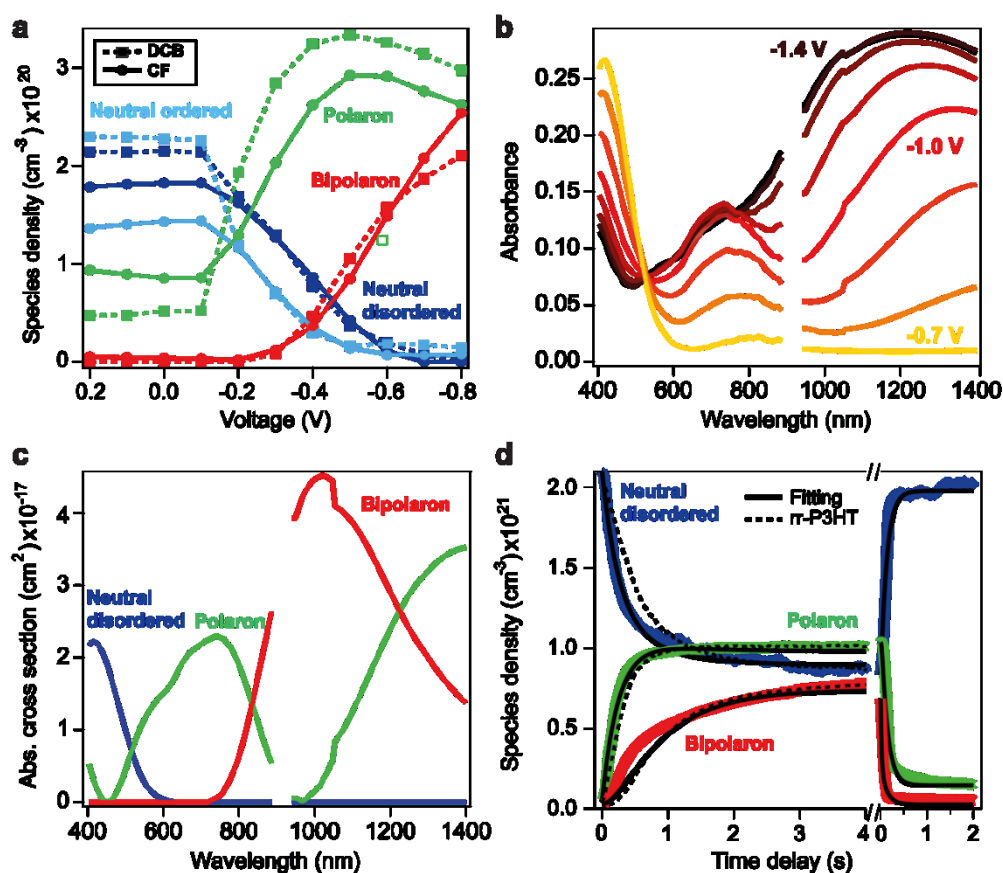
WILEY-VCH

Figure 5: a) MCR species densities as a function of doping voltage for regioregular P3HT films cast from 1,2-dichlorobenzene (DCB, squares with dashed lines) and chloroform (CF, circles with solid lines), from VIS/NIR spectro-electrochemistry in aqueous KPF$_6$ electrolyte (0.1 mol L^{-1}) measured in 'OECT-like' devices. b) Steady-state absorbance spectra of a 120 nm regiorandom RRa-P3HT film cast on ITO substrate upon application of doping voltages ranging from -0.7 V to -1.4 V (ΔV = -0.1 V) in KPF$_6$/acetonitrile electrolyte. c) Corresponding spectral signatures of each species obtained from the MCR analysis. d) Time-resolved species concentrations obtained for the RRa-P3HT film upon application of (left) a doping step from 0 V to -1.2 V and (right) a dedoping step back to 0 V. For comparison, the doping dynamics to -0.6 V (similar overpotential) of a regioregular P3HT film (rr-P3HT) cast from chloroform are shown.
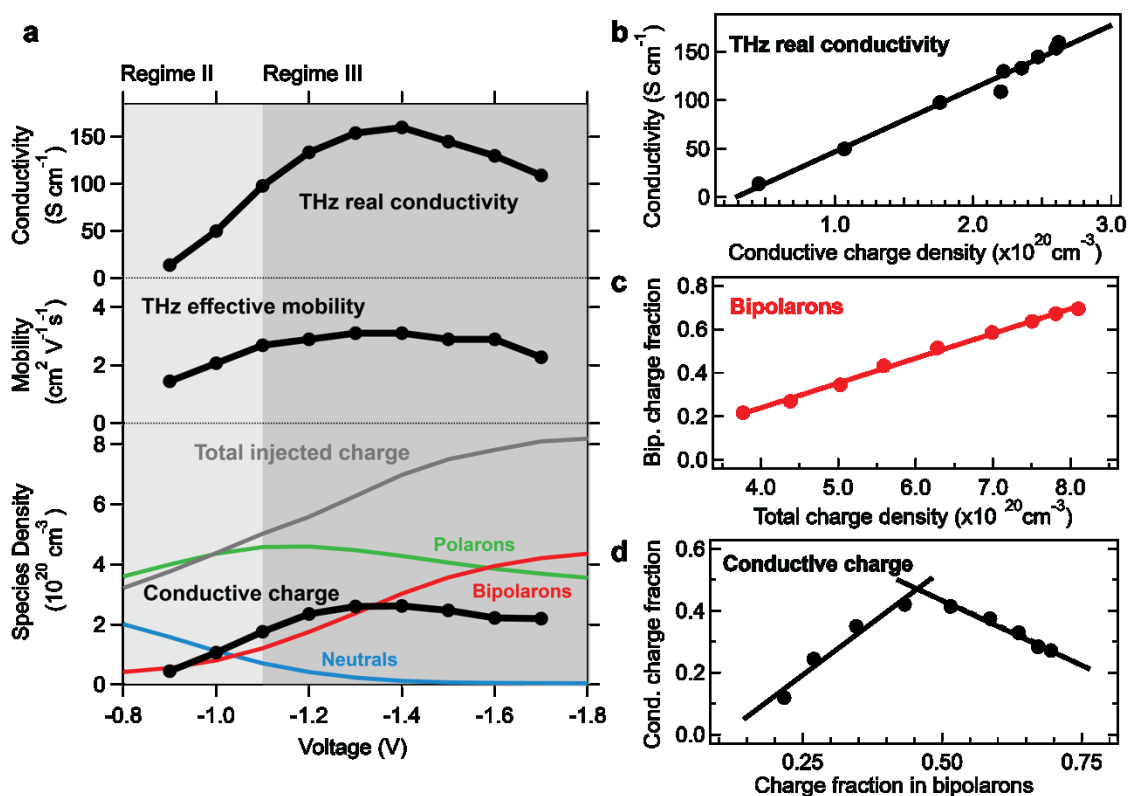
WILEY-VCH

Figure 6. a) THz conductivity parameters obtained *in-situ* for a ~270 nm thick regioregular P3HT film cast from 1,2-dichlorobenzene in an OECT-like device in TBAPF$_6$/acetonitrile electrolyte. The real conductivity at 1 THz (top), the effective mobility obtained from Drude-Smith analysis (middle), and the density of conductive charges (also from Drude-Smith analysis, bottom) are shown as thick black lines with round markers. In addition, the density of the different redox species (from Vis/NIR spectroelectrochemistry and MCR analysis on the same device) is indicated at the bottom. The total injected charge density is calculated as the polaron plus twice the bipolaron density (P+2B). b) Real conductivity at 1 THz as a function of conductive charge density. c) Fraction of charge in bipolarons (2B/(2B+P)) as a function of the injected charge density. d) Fraction of conductive charge as a function of the fraction of charge in bipolarons. Solid lines in b)-d) are guides to the eye.

Table 1: Rate constants (k in s^{-1}) and equilibrium constants (K, unitless) for the electrochemical **doping** of P3HT upon switching from +0.4 V to different doping voltages at -0.1 V to -0.8 V, obtained via kinetic modelling. The equilibrium constants are defined as the forward rate constant divided by the backward rate constant.

Voltage (V):	- 0.1	- 0.2	- 0.3	- 0.4	- 0.5	- 0.6	- 0.7	- 0.8
$k_{N,ord \rightarrow P,ord}$	0.01	0.16	0.47	1.09	2.07	3.05	3.88	4.29
$K_{N,ord \rightleftharpoons P,ord}$	0.17	0.60	1.52	3.99	13.94	∞	∞	∞
$k_{P,ord \rightarrow B,ord}$						0.004	0.01	0.02
$K_{P,ord \rightleftharpoons B,ord}$						0.08	0.22	0.32
$k_{N,dis \rightarrow P,dis}$	0.01	0.07	0.23	0.48	0.93	1.30	1.48	1.62
$K_{N,dis \rightleftharpoons P,dis}$	0.06	0.20	0.37	0.66	1.18	2.27	4.97	12.50
$k_{P,dis \rightarrow B,dis}$			0.07	0.21	0.58	1.13	1.33	1.34
$K_{P,dis \rightleftharpoons B,dis}$			0.16	0.30	0.55	0.92	1.37	1.65

Table 2: Rate constants (k in s^{-1}) and equilibrium constants (K, unitless) for the electrochemical **dedoping** of P3HT upon switching from different doping voltages (-0.1 V to -0.8 V) to a dedoping voltage of +0.4 V, obtained via kinetic modelling. The equilibrium constants are defined as the forward rate constant divided by the backward rate constant.

Voltage (V):	- 0.1	- 0.2	- 0.3	- 0.4	- 0.5	- 0.6	- 0.7	- 0.8
$k_{B,ord \rightarrow P,ord}$						18.66	15.88	10.08
$k_{P,ord \rightarrow N,ord}$	3.82	3.48	3.12	2.68	2.27	1.77	1.29	0.97
$K_{P,ord \rightleftharpoons N,ord}$	23.21	18.97	15.65	13.07	12.05	12.05	12.05	9.07

$k_{B,dis \to P,dis}$			8.63	8.63	8.63	6.01	4.60	3.93
$k_{P,dis \to N,dis}$	1.72	2.75	3.34	4.85	6.07	4.49	4.24	2.98
$K_{P,dis \rightleftharpoons N,dis}$	∞	∞	∞	∞	202.45	56.85	31.96	31.96

References

[1] a)J. H. Kim, S.-M. Kim, G. Kim, M.-H. Yoon, *Macromol. Biosci.* **2020**, 20, 2000211; b)M. Łapkowski, A. Proń, *Synth. Met.* **2000**, 110, 79; c)H. J. Lee, S.-M. Park, *J. Phys. Chem. B* **2004**, 108, 1590.

[2] a)Y. van de Burgt, E. Lubberman, E. J. Fuller, S. T. Keene, G. C. Faria, S. Agarwal, M. J. Marinella, A. Alec Talin, A. Salleo, *Nat. Mater.* **2017**, 16, 414; b)Y. Tuchman, T. N. Mangoma, P. Gkoupidenis, Y. van de Burgt, R. A. John, N. Mathews, S. E. Shaheen, R. Daly, G. G. Malliaras, A. Salleo, *MRS Bulletin* **2020**, 45, 619.

[3] a)W. Yao, L. Shen, P. Liu, C. Liu, J. Xu, Q. Jiang, G. Liu, G. Nie, F. Jiang, *Mater. Chem. Front.* **2020**, 4, 597; b)H. Ito, H. Mada, K. Watanabe, H. Tanaka, T. Takenobu, *Commun. Phys.* **2021**, 4, 8.

[4] a)D. Moia, A. Giovannitti, A. A. Szumska, I. P. Maria, E. Rezasoltani, M. Sachs, M. Schnurr, P. R. F. Barnes, I. McCulloch, J. Nelson, *Energy Environ. Sci* **2019**, 12, 1349; b)X. Wang, J. Zhou, W. Tang, *Mater. Horiz.* **2021**, 8, 2373.

[5] a)J. Rivnay, S. Inal, A. Salleo, R. M. Owens, M. Berggren, G. G. Malliaras, *Nat. Rev. Mater.* **2018**, 3, 17086; b)D. T. Duong, Y. Tuchman, P. Chakthranont, P. Cavassin, R. Colucci, T. F. Jaramillo, A. Salleo, G. C. Faria, *Adv. Electron. Mater.* **2018**, 4, 1800090; c)J. Rivnay, R. M. Owens, G. G. Malliaras, *Chem. Mater.* **2014**, 26, 679.

[6] R. Colucci, H. F. d. P. Barbosa, F. Günther, P. Cavassin, G. C. Faria, *Flex. Print. Electron.* **2020**, 5, 013001.

[7] a)P. Shiri, D. Neusser, C. Malacrida, S. Ludwigs, L. G. Kaake, *J. Phys. Chem. C* **2021**, 125, 536; b)B. D. Paulsen, R. Wu, C. J. Takacs, H.-G. Steinrück, J. Strzalka, Q. Zhang, M. F. Toney, J. Rivnay, *Adv. Mater.* **2020**, 32, 2003404; c)C. Enengl, S. Enengl, S. Pluczyk, M. Havlicek, M. Lapkowski, H. Neugebauer, E. Ehrenfreund, *ChemPhysChem* **2016**, 17, 3836; d)D. Neusser, C. Malacrida, M. Kern, Y. M. Gross, J. van Slageren, S. Ludwigs, *Chem. Mater.* **2020**, 32, 6003; e)D. Rawlings, E. M. Thomas, R. A. Segalman, M. L. Chabinyc, *Chem. Mater.* **2019**, 31, 8820; f)E. M. Thomas, M. A. Brady, H. Nakayama, B. C. Popere, R. A. Segalman, M. L. Chabinyc, *Adv. Funct. Mater.* **2018**, 28, 1803687; g)J. Nightingale, J. Wade, D. Moia, J. Nelson, J.-S. Kim, *J. Phys. Chem. C* **2018**, 122, 29129.

[8] J. O. Guardado, A. Salleo, *Adv. Funct. Mater.* **2017**, 27, 1701791.
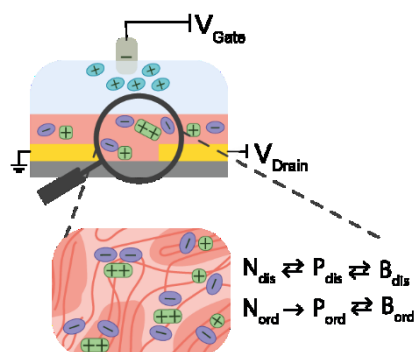
WILEY-VCH

WILEY-VCH

[9]   A. E. Mansour, A. M. Valencia, D. Lungwitz, B. Wegner, N. Tanaka, Y. Shoji, T. Fukushima, A. Opitz, C. Cocchi, N. Koch, *Phys. Chem. Chem. Phys.* **2022**, 24, 3109.

[10]   D. Tsokkou, P. Cavassin, G. Rebetez, N. Banerji, *Mater. Horiz.* **2022**, 9, 482.

[11]   L. Q. Flagg, R. Giridharagopal, J. Guo, D. S. Ginger, *Chem. Mater.* **2018**, 30, 5380.

[12]   J.-F. Chang, B. Sun, D. W. Breiby, M. M. Nielsen, T. I. Sölling, M. Giles, I. McCulloch, H. Sirringhaus, *Chem. Mater.* **2004**, 16, 4772.

[13]   a)V. Vijayakumar, Y. Zhong, V. Untilova, M. Bahri, L. Herrmann, L. Biniek, N. Leclerc, M. Brinkmann, *Adv. Energy Mater.* **2019**, 9, 1900266; b)J. Clark, J.-F. Chang, F. C. Spano, R. H. Friend, C. Silva, *Appl. Phys. Lett.* **2009**, 94, 163306; c)J. Clark, C. Silva, R. H. Friend, F. C. Spano, *Phys. Rev. Lett.* **2007**, 98, 206406.

[14]   a)J. L. Bredas, G. B. Street, *Acc. Chem. Res.* **1985**, 18, 309; b)E. C. Wu, C. Z. Salamat, O. L. Ruiz, T. Qu, A. Kim, S. H. Tolbert, B. J. Schwartz, *Adv. Funct. Mater.* **2023**.

[15]   I. Sahalianov, J. Hynynen, S. Barlow, S. R. Marder, C. Müller, I. Zozoulenko, *J. Phys. Chem. B* **2020**, 124, 11280.

[16]   a)M. Skompska, A. Szkurłat, *Electrochim. Acta* **2001**, 46, 4007; b)G. Heimel, *ACS Cent. Sci.* **2016**, 2, 309; c)M. B. Qarai, R. Ghosh, F. C. Spano, *J. Phys. Chem. C* **2021**, 125, 24487; d)D. Tsokkou, L. Peterhans, D. X. Cao, C.-K. Mai, G. C. Bazan, T.-Q. Nguyen, N. Banerji, *Adv. Funct. Mater.* **2020**, 30, 1906148.

[17]   A. Savva, R. Hallani, C. Cendra, J. Surgailis, T. C. Hidalgo, S. Wustoni, R. Sheelamanthula, X. Chen, M. Kirkus, A. Giovannitti, A. Salleo, I. McCulloch, S. Inal, *Adv. Funct. Mater.* **2020**, 30, 1907657.

[18]   J. Hynynen, D. Kiefer, L. Yu, R. Kroon, R. Munir, A. Amassian, M. Kemerink, C. Müller, *Macromolecules* **2017**, 50, 8140.

[19]   W. T. Choi, A. J. Bard, *J. Phys. Chem. C* **2020**, 124, 3439.

[20]   a)W. C. Tsoi, S. J. Spencer, L. Yang, A. M. Ballantyne, P. G. Nicholson, A. Turnbull, A. G. Shard, C. E. Murphy, D. D. C. Bradley, J. Nelson, J.-S. Kim, *Macromolecules* **2011**, 44, 2944; b)V. Untilova, T. Biskup, L. Biniek, V. Vijayakumar, M. Brinkmann, *Macromolecules* **2020**, 53, 2441.

[21]   X. Shen, W. Hu, T. P. Russell, *Macromolecules* **2016**, 49, 4501.

[22]   M. Arvind, C. E. Tait, M. Guerrini, J. Krumland, A. M. Valencia, C. Cocchi, A. E. Mansour, N. Koch, S. Barlow, S. R. Marder, J. Behrends, D. Neher, *J. Phys. Chem. B* **2020**, 124, 7694.

WILEY-VCH

[23]   a)J. Yamamoto, Y. Furukawa, *Org. Electron.* **2016**, 28, 82; b)J. Yamamoto, Y. Furukawa, *J. Phys. Chem. B* **2015**, 7.

[24]   W. C. Tsoi, D. T. James, J. S. Kim, P. G. Nicholson, C. E. Murphy, D. D. C. Bradley, J. Nelson, J.-S. Kim, *J. Am. Chem. Soc.* **2011**, 133, 9834.

[25]   a)P. Shiri, E. J. S. Dacanay, B. Hagen, L. G. Kaake, *J. Mater. Chem. C* **2019**, 7, 12935; b)P. Shiri, E. J. S. Dacanay, B. Hagen, L. G. Kaake, *J. Phys. Chem. C* **2019**, 123, 19395.

[26]   R. Wu, B. D. Paulsen, Q. Ma, J. Rivnay, *Chem. Mater.* **2022**, 34, 9699.

[27]   L. Peterhans, E. Alloa, Y. Sheima, L. Vannay, M. Leclerc, C. Corminboeuf, S. C. Hayes, N. Banerji, *Phys. Chem. Chem. Phys.* **2017**, 19, 28853.

[28]   G. Rebetez, O. Bardagot, J. Affolter, J. Réhault, N. Banerji, *Adv. Funct. Mater.* **2022**, 32, 2105821.

[29]   M. Roelfs, P. C. Kroon, Zenodo, 2020.

[30]   T.-A. Chen, X. Wu, R. D. Rieke, *J. Am. Chem. Soc.* **1995**, 117, 233.

[31]   D. T. Scholes, P. Y. Yee, J. R. Lindemuth, H. Kang, J. Onorato, R. Ghosh, C. K. Luscombe, F. C. Spano, S. H. Tolbert, B. J. Schwartz, *Adv. Funct. Mater.* **2017**, 27, 1702654.

[32]   D. Tsokkou, P. Cavassin, G. Rebetez, N. Banerji, *Mater. Horiz.* **2022**.

[33]   G. Zotti, G. Schiavon, *Chem. Mater.* **1991**, 3, 62.

[34]   D. Tsokkou, P. Cavassin, G. Rebetez, N. Banerji, in *Boris*, http://10.48350/165169 2022.

[35]   M.-J. Sher, J. A. Bartelt, T. M. Burke, A. Salleo, M. D. McGehee, A. M. Lindenberg, *Adv. Electron. Mater.* **2016**, 2, 1500351.

[36]   a)J. Joo, S. M. Long, J. P. Pouget, E. J. Oh, A. G. MacDiarmid, A. J. Epstein, *Phys. Rev. B* **1998**, 57, 9567; b)H. Tanaka, K. Kanahashi, N. Takekoshi, H. Mada, H. Ito, Y. Shimoi, H. Ohta, T. Takenobu, *Sci. Adv.* **2020**, 6, eaay8065.

[37]   M. Koopmans, M. A. T. Leiviskä, J. Liu, J. Dong, L. Qiu, J. C. Hummelen, G. Portale, M. C. Heiber, L. J. A. Koster, *ACS Appl. Mater. Interfaces* **2020**, 12, 56222.

[38]   E. Stein, O. Nahor, M. Stolov, V. Freger, I. M. Petruta, I. McCulloch, G. L. Frey, *Nat. Commun.* **2022**, 13, 5548.

[39]   P. Krauspe, N. Banerji, J. Réhault, *J. Opt. Soc. Am. B* **2020**, 37, 127.

WILEY-VCH

[40]   C. H. Camp, *J. Res. Natl. Inst. Stand. Technol.* **2019**, 124, 124018.

Accepted Article

TOC Entry

Novel organic bioelectronic technologies rely on the efficient electrochemical doping of conjugated polymers. In this work, we investigate how the doping process can be controlled by the co-existence of ordered and disordered domains in polymeric films. We show that both domains are doped trough different mechanisms and extents, and that optimal conductivity can be achieved by modulating film order.

$$N_{dis} \rightleftarrows P_{dis} \rightleftarrows B_{dis}$$
$$N_{ord} \rightarrow P_{ord} \rightleftarrows B_{ord}$$